Preprints.org

Article

Evaluation of Porosity in AISI 316L Samples Processed by Laser-Powder Directed Energy Deposition

Alessandro Salmi [*] , Gabriele Piscopo , Eleonora Atzeni , Adriano Nicola Pilagatti

Article

Evaluation of Porosity in AISI 316L Samples Processed by Laser-Powder Directed Energy Deposition

Alessandro Salmi *[ID], **Gabriele Piscopo** [ID], **Eleonora Atzeni** [ID] **and Adriano Nicola Pilagatti** [ID]

Department of Management and Production Engineering (DIGEP), Politecnico di Torino, Corso Duca degli Abruzzi 24, 10129 Torino, Italy; gabriele.piscopo@polito.it (G.P.); eleonora.atzeni@polito.it (E.A.); adriano.pilagatti@polito.it (A.P.)

* Correspondence: alessandro.salmi@polito.it; Tel.:+39-011-090-7263

Abstract: Laser-Powder Directed Energy Deposition (DED-LB/Powder) is an additive manufacturing process that is gaining popularity in the manufacturing industry due to its numerous advantages, particularly in repairing operations. However, its application is often limited to case studies due to some critical issues that need to be addressed, such as the degree of internal porosity. This paper investigates the effect of the most relevant process parameters of the DED-LB/Powder process on the level and distribution of porosity. Results indicate that, among the process parameters examined, porosity is less affected by travel speed and more influenced by powder mass flow rate and laser power. Additionally, a three-dimensional finite element transient model was introduced, which was able to predict the development and location of lack-of-fusion pores along the building direction.

Keywords: additive manufacturing; process parameters; laser powder directed energy deposition; porosity; FE simulation; 316L

1. Introduction

Additive Manufacturing (AM) processes have already been adopted by many industrial sectors such as biomedical, energy, oil & gas, aerospace and nuclear [1]. The interest in AM over conventional manufacturing methods is driven by several advantages in terms of geometrical complexity, material usage, time saving and added value [2]. Among the metal AM processes, Directed Energy Deposition (DED) processes are currently at the forefront of innovation. As a matter of fact, the revenue market shares of Powder Bed Fusion (PBF) and DED processes in 2019 were around 85 % and 8.3 % respectively; by 2025 the revenue of PBF processes is expected to fall to 63 %, while the DED processes will rise to 11.1 % [3]. The possibility to produce large components (length bigger than one meter), to change the material during the process realizing multi-graded materials, and to repair components by depositing directly onto an existing planar or non-planar surface are only a few of the main advantages of the DED processes over PBF or conventional processes [4,5]. Hence, focusing the attention on DED processes, the ASTM standard [6] classifies the different variants with respect to the heat sources (laser, electron beam or plasma arc) and to the feedstock material (powder or wire). In more specific terms, the DED process that uses a laser as a energy source and a powder as a feedstock material is the most used [7] and this process is referred as DED-LB/Powder [7,8]. Despite the enormous potentialities, the industrial application of the DED-LB/Powder process is still limited [7] and one of the main reasons is that the components produced are prone to a high level of porosity [9]. The presence of pores negatively affects both the density and the mechanical characteristics such as the yield strength, the ultimate tensile strength, and the Young's modulus [10]. In addition, they can act as stress concentrators and crack growth sites [11]. Hence, several efforts are needed to understand and minimize the porosity level that arises from the deposition process.

The literature distinguishes three basic types of pores in DED components: (a) keyhole, (b) gas-induced and (c) lack-of-fusion pores, which result from different mechanisms [12,13]. Specifically, keyhole pores appear elongated along the building direction [12] and result from material evaporation. They are typically the consequence of unstable melt pool dynamics at high energy density [14]. Gas-induced pores, instead, are spherical in shape and smaller, and are usually caused by the presence of gas in the feedstock material [15], selective evaporation of an element of the specific alloy [16] or by the

entrapment of the shielding gas [13]. Finally, lack-of-fusion pores are characterized by an elongated irregular shape and their size is comparable to the melt pool scale [12] and arise from an inadequate penetration of the melt pool into the substrate due to insufficient energy [9]. Focusing the attention on gas-induced and lack-of-fusion pores, it was observed that the first ones are mainly located inside the deposited track and they are mostly influenced by the melt pool depth, while the latter are influenced by melt pool width and occur at the interface between two consecutive tracks [17].

Susan et al. [18] and Ahsan et al. [19] showed an important relation between the powder production method and the sample porosity. It was observed that the porosity of the powder particles and the shape of the powder were directly related to the powder production method, and that these factors influenced the porosity level of the produced samples. As a rule of thumb, it is a good practice to characterize the feedstock material prior to deposition. Rahman Rashid et al. [20] observed porosities of the order of 5 µm to 15 µm in AISI 316L single layers. These porosities were mainly located at both ends of each track due to the gas entrapped into the melt pool. By characterizing the porosity of AISI 316L samples, Tan et al. [11], found that the part density was not uniform, but the samples were denser in the upper zone farthest from the substrate. Small and almost spherical pores were prevalent in that area. Bottom zone porosity in these samples was greater than 150 µm in diameter. Besides, Zheng et al. [21] showed that the lack-of-fusion pores occurring at the layer boundaries were correlated with an improper Z-increment combined with the selected process parameters, resulting in reduced part growth which caused the laser to be out of focus. Consequently, the most straightforward approach used in the literature to minimize the porosity level is to adjust the process parameters, namely laser power, travel speed, hatching distance and powder mass flow rate [8,12,22].

Several works are present in the literature about the effect of process parameters on part porosity. Amar et al. [23] produced $10 \times 10 \times 10 \, mm^3$ AISI 316L samples and using a response surface methodology observed that the most significant parameter influencing the porosity was the powder mass flow rate; in detail, the porosity increased with powder mass flow rate due to track overgrowing. Majumdar et al. [24] observed that porosity increased when powder mass flow rate values were too low or too high. Analogously, Lin et al. [25] showed that for low values of powder mass flow rate, the energy provided to the material was higher and this led to a higher quantity of gas-induced pore. Increasing the powder mass flow rate, firstly a reduction of porosity was observed however, for a higher powder mass flow rate, the porosity increased due to lack-of-fusion pores.

As for laser power and travel speed, the literature on the topic of porosity presents contrasting points of view. During the deposition of AISI 316L thin walls, Majumdar et al. [24] observed that porosity decreased with increasing travel speed and was almost independent from laser power. On the contrary, Kartikeya Sarma et al. [26] in the deposition of AISI 316L cylinder ($\Phi 10 \times 25 \, mm^3$) showed that the porosity was mainly influenced by laser power but the effect of travel speed and powder mass flow rate was less significative. Savitha et al. [27] highlighted that the porosity was significantly influenced by the interaction between laser power and travel speed. Lin et al. [25] performing a three one-factor-at-a-time experiment on AISI 316L cylindrical thin walls observed that porosity decreased with increasing the laser power up to 1800 W however for higher laser power the porosity slightly increased. Amar et al. [23] observed that the laser power and the travel speed did not significantly affect the porosity.

This analysis of the literature highlights, as confirmed by several reviews [5,8,28,29], the complexity of the phenomena governing the DED-LB/Powder process. Numerical simulation coupled with experiments can be used to deepen the understanding of the DED-LB/Powder process. More specifically, the macro-scale approaches typically used to study the temperature distribution and the thermal cycles during the deposition process, which are able to predict the microstructure evolution and the residual stresses [30], could be extended to the analysis of porosity in analogy to casting simulations [12,28,31].

In this work, firstly a characterization of pores in AISI 316L massive samples using a Computed Tomography (CT) analysis was performed and the effect of the main process parameters was evaluated.

The pores characterization was obtained considering their position, their size and their shape. Then, a macro-scale three-dimensional Finite Element (FE) thermal model was adopted in order to evaluate its feasibility in forecasting the probability and location of pores in DED samples.

2. Materials and Methods

The following subsections describe the experimental procedure adopted in this work. Firstly, the sample geometry and the equipment used for samples production and characterization are illustrated. Then, the selection of the process parameters and their values in the experimental tests are detailed. Finally, the thermal numerical model is presented.

2.1. Sample Geometry, Production and Characterization

AISI 316L parallelepiped samples with dimensions of $10 \times 20 \times 20 \, \text{mm}^3$ were deposited on substrates of the same material. The geometry is illustrated in Figure 1. In this work, MetcoAdd 316L gas atomized powder provided by Oerlikon Metco Inc. (Troy, MI, US) was used. Powder particles had an almost spherical shape with few satellites and the diameter ranging from 45 µm to 106 µm. A detailed characterization of the powder particles is reported in [32]. The production of the samples was performed on a LASERDYNE® 430 by Prima Additive (Collegno, Italy). This DED-LB/Powder system is equipped with a 1000 W fiber laser. The laser beam has a top-hat distribution and the nominal diameter is 2 mm at the focal plane. The deposition head includes 4 coaxial nozzles which generate a Gaussian powder flow with a diameter of around 4 mm at the focal plane of the laser. The powder particles are delivered in the working area by means of a constant flux of Argon.
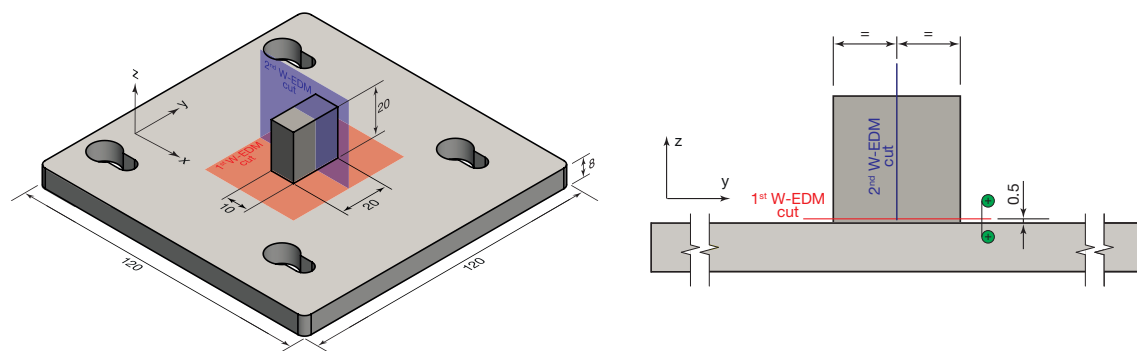

Figure 1. Geometry and dimensions of the sample.

The process parameters recognized in the literature as the most relevant [4,8,29] were considered, namely travel speed (v), powder mass flow rate (Q_P), and laser power (P). Specifically, a one-factor design was used to test the effect of process parameters individually and identify critical parameters for porosity. Consequently, three sets of samples were produced, one for each parameter tested. As a starting point for the design of experiment, the parameter values previously utilized for the production of AISI 316L bulk samples using the same DED-LB/Powder system were employed [33], which had resulted in satisfactory outcomes in terms of dimensional accuracy. In detail, the process parameter values were: $P = 500 \, \text{W}$, $Q_P = 4.5 \, \text{g/min}$, and $v = 850 \, \text{mm/min}$, and will be referred to as reference values.

Initially, due to its relevance, the effect on the porosity of an increased laser power value was tested. Three levels of laser power were considered, leading to a first set of samples. Then, the effect of an increased powder mass flow rate was tested, to evaluate its influence on porosity at the best laser power level determined from the first set (Set 1). The samples realized by only varying the powder mass flow rate were the second set of samples to be analyzed (Set 2). Finally, the less porous sample was selected to evaluate the effect of a variation of the travel speed. This was the third and last set of samples (Set 3). Table 1 lists the values of process parameters analyzed in this work. Other process parameters were always kept constant during the production process. In detail, a hatching distance

of 1 mm, a Z-increment of 0.5 mm and a stand-off distance of 7.5 mm were used. The deposition was performed using a raster deposition strategy with a rotation of 90° at each layer, and a contour path with the same process parameters as the core.

Table 1. Process parameter variables and their values (the bold values are the reference values).

Process parameter	Values
Laser power, P (W)	**500** – 650 – 800
Powder mass flow rate, Q_P (g/min)	**4.5** – 6.0
Travel speed, v (mm/min)	**850** – 900 – 950

After the production, samples were removed from the substrate through the Wire-Electrical Discharge Machining (W-EDM) system by Suzhou Baoma (Suzhou, China). Subsequently, samples were split into two halves, left and right, and subjected to CT. The CT acquisition was performed on a Phoenix V | tome | x S240 by Baker Hughes (Houston, TX, USA). The parameter values set during CT acquisition, in combination with the dimensions of the split sample, allowed for a good balance between sample and background gray values. This resulted in a voxel size of 22.5 μm. The acquisition was performed capturing 1500 images in a full 360° rotation. The process parameter values used during CT scans are listed in Table 2.

Table 2. Setup and process parameters used during Computed Tomography acquisition.

CT process parameter	Values
Voltage, V (kV)	200
Current, I (μA)	110
Filter	0.5 mm of copper
Timing (ms)	333
Averaging	3
Skip frames	2

After the acquisition, the raw data was processed using Phoenix datos | x 2 reconstruction software to remove spurious information and compensate for possible sample and detector drifts. Then, the corrected data was introduced into the software VGSTUDIO MAX 3.5 developed by Volume Graphics (Heidelberg, Germany) in order to perform the porosity analysis. In detail, after the determination of the external surface from the CT histogram using an ISO value of 50 %, which corresponds to the mean value between the background gray value and the material gray value, the VGDefX/Only threshold algorithm was used in order to detect the internal defects by comparing the gray values between two adjacent voxels. In the algorithm, the material definition was performed using the determined surface and setting an interpolation threshold factor of 1.05. The material definition was then used to define the maximum gray value of voids. Based on the voxel size, defects were considered to be present if their size exceeded 45 μm, which is equivalent to two voxels.

2.2. Three-Dimensional Numerical Thermal Model

In order to relate the porosity developed during the DED-LB/Powder process with the thermal history and temperature distribution in the samples, a thermal three-dimensional numerical model was used. The model was implemented in Abaqus/Standard 2023 by Dassault Systèmes® and the geometry, illustrated in Figure 2, consisted of a substrate (gray geometry) with dimensions of $120 \times 120 \times 8 \, mm^3$ and an activation volume (light blue geometry) with overall dimensions of $30 \times 30 \times 30 \, mm^3$. The activation volume represents and simulates the overall material that can be deposited during the DED-LB/Powder process and is larger than the geometry of $10 \times 20 \times 20 \, mm^3$ to be activated. At the beginning of the analysis, the elements of the activation volume are not included in the computational

domain and an activation strategy is required. The activation strategy, which is used to progressively add elements of the activation volume into the computational domain simulating the addition of material during the process, is based on the UEPACTIVATIONVOL user subroutine. A detailed explanation of the subroutine and how it works is reported in [34].

The geometry was discretized using a structured mesh with 20-node quadratic heat transfer elements (DC3D20 type) and consisted of a finer mesh in the activation volume and a coarser mesh in the substrate. The resulting mesh is shown in Figure 2. This discretization strategy allowed to obtain a good balance between the computational time and the resolution and the accuracy of the results. Specifically, the elements of the activation volume were 1 mm wide, 1 mm long and 0.5 mm height. In the substrate, starting from the deposition area, the mesh size was gradually increased and the maximum element dimensions were 15.4 mm in width, 15.4 mm long and 4.4 mm in height.
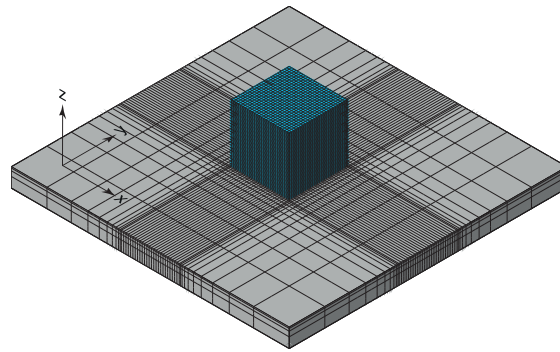

Figure 2. Mesh discretization of the model: the gray volume represents the substrate, the blue volume represents the volume used by the activation strategy.

The transient temperature distribution $T(x, y, z, t)$ is calculated by solving the general heat conduction equation without energy generation, reported in Equation (1):

$$\rho c_p \frac{\partial T}{\partial t} = \frac{\partial}{\partial x}\left(k\frac{\partial T}{\partial x}\right) + \frac{\partial}{\partial y}\left(k\frac{\partial T}{\partial y}\right) + \frac{\partial}{\partial z}\left(k\frac{\partial T}{\partial z}\right) \tag{1}$$

where ρ is the material density, c_p is the heat capacity, k is the thermal conductivity.

The boundary conditions allow the effect of the moving heat source and the phenomena of convection and radiation to be added in the numerical model. They are expressed by Equation (2):

$$-k(\nabla T \cdot \boldsymbol{n})|_\Pi = \begin{cases} I_L(x, y, z, t) - h_c(T - T_0) - \epsilon_r \sigma(T^4 - T_0^4) & \text{if } \Pi \in \Pi_L \\ -h_c(T - T_0) - \epsilon_r \sigma(T^4 - T_0^4) & \text{if } \Pi \notin \Pi_L \end{cases} \tag{2}$$

where Π is the heat exchange surface, $\boldsymbol{n}$ is the normal vector to the surface Π, $I_L(x, y, z, t)$ is the intensity provided by the laser beam, h_c is the specific heat coefficient, ϵ_r is the surface emissivity, σ is the Stefan-Boltzmann constant, and Π_L is the surface interested by the laser beam. Two different initial conditions were defined at the substrate and to the activation volume. At the beginning of the process at the time $t = 0$, the substrate was at ambient temperature, hence the initial condition for the elements of the substrate was defined by Equation (3):

$$T(x, t, z, t = 0) = T_0 \tag{3}$$

The initial condition for the elements that were introduced in the numerical domain at the time $t = t_{act}$ is defined by Equation (4). This condition considers the temperature increment of powder particles caused by energy absorption during the in-flight time.

$$T(x, t, z, t = t_{act}) = T_{act} \tag{4}$$

2.2.1. Assumptions and Material Properties

The mesoscale model previously developed by Piscopo et al. [34] was adapted to a macro-scale level in this work. Especially, some assumptions were introduced in order to limit the computational time required to obtain the desired results and these assumptions are strictly dependent on the macro-scale simulation approach.

Firstly, since the prediction of the melt pool and track dimensions are out of the scope of a macro-scale simulation, the track width was assumed to be equal to the laser beam diameter and the height equal to the Z-increment.

The reduction of laser power due to absorption, scattering and reflection phenomena of powder mass flow rate and substrate was taken into account by a correction coefficient β of 0.4 [35] that was used to reduce the laser intensity. Activation temperature, which simulates the temperature of powder particles just before they enter the melt pool is a critical factor in the micro-scale and meso-scale approaches since the initial thermal gradient highly influences the melt pool behavior and phenomena. In a macro-scale approach, in which the production of a whole component is analyzed, the thermal energy provided by the powder particles is negligible with respect to the energy provided by the laser beam during the process. For this reason, the activation temperature was set to be equal to the ambient temperature.

According to Gouge et al. [36] in the deposition area turbulent flows are generated by the shielding gas, hence a forced convection should be considered. In this work, it was assumed that the forced convection acted on the deposited material and on the upper surface of the substrate. On the lateral and the bottom surfaces of the substrate natural convection was considered. The values of forced and natural convection were set to $40\,\mathrm{W/(m^2\,K)}$ and $10\,\mathrm{W/(m^2\,K)}$ respectively. The emissivity value was 0.6.

Temperature-dependent material properties of AISI 316L were used. Figure 3 shows the values of density, specific heat and thermal conductivity as a function of the temperature [34]. In addition, the phase transformation was considered by including in the model the latent heat of fusion and the non-equilibrium temperatures.
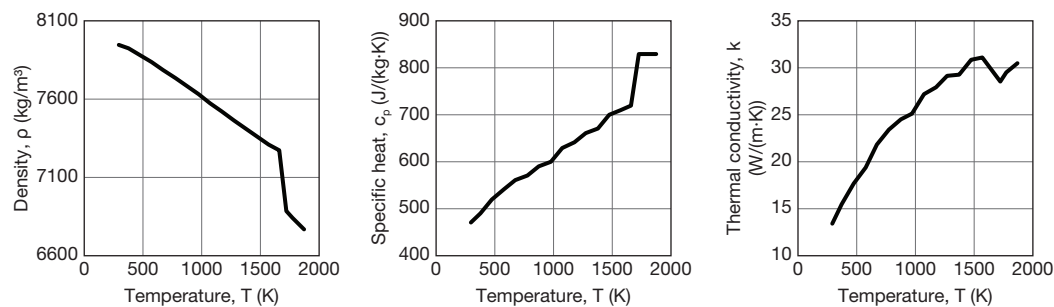

Figure 3. AISI 316L stainless steel temperature-dependent thermal material properties.

3. Results

In the following, the results of the experimental campaign are discussed in terms of porosity evaluated by CT analysis. The thermal behavior resulting from the numerical simulation allowed to correlate porosities and thermal history, and results are presented in the final subsection.

3.1. Porosity Analysis and Effect of Process Parameters

For each sample, both halves were analyzed to provide repeatability data. Good repeatability was observed with a maximum deviation of ± 0.01 for the porosity. In the following, the results refer to the left half of each sample. The porosity results are summarized in Table 3. In general, it was observed that, among the process parameters, the laser power mostly affected the overall porosity value, with porosity decreasing from 0.26 % to 0.07 % as the laser power was increased from 500 W to 650 W. A further increase of laser power did not alter the porosity value however, other mechanisms

were observed as detailed in Section 3.1.1. CT scans revealed that the increase in the powder mass flow rate from $4.5\,\mathrm{g/min}$ to $6.0\,\mathrm{g/min}$ worsened porosity, which increased from $0.07\,\%$ to $0.10\,\%$. As regards the travel speed, it was noted that the porosity level was not significantly influenced by the value of travel speed and was on average $0.07\,\%$ at $P = 650\,\mathrm{W}$ and $Q_P = 4.5\,\mathrm{g/min}$.

Table 3. Process parameters (the bold values are the reference values) and resulting porosities.

Deposits	P (W)	Q_P (g/min)	v (mm/min)	Porosity (%)
Set 1	**500** 650* 800	**4.5**	**850**	0.26 0.07 0.07
Set 2	650*	**4.5*** 6.0	**850**	0.07 0.10
Set 3	650*	**4.5***	**850*** 900 950	0.07 0.07 0.08

Note: * best parameter value in the set.

3.1.1. Effect of Laser Power

Figure 4a illustrates samples produced with different levels of laser power. It was observed that despite all the samples were successfully produced, the sample realized with the lower laser power, that was $500\,\mathrm{W}$, was characterized by uneven deposition and powder agglomeration on the external surface, especially in the bottom area. These defects were attributed to the low specific energy [37]. In fact, to improve surface quality, typical deposition strategies include a contour path with a higher energy density than that used for core hatching. Contouring at higher specific energy has also the effect of reducing the surface defects that were identified in the experiments performed with the contour pass at the same energy density as the core. The porosity level measured in this sample was $0.26\,\%$, the highest measured in the experiments, as reported in Table 3. The degree of internal porosity implies that the laser power and the corresponding energy density were inadequate to produce a fully dense sample. Gas-induced pores and lack-of-fusion pores were observed in the CT scan images. While the gas-induced pores were randomly distributed in the analyzed volume, the lack-of-fusion pores were concentrated in the bottom part of the samples. Lack-of-fusion pores are a direct consequence of low specific energy and low substrate temperature. In fact, at the beginning of the deposition process, the deposition is performed on a substrate at ambient temperature and the heat transfer is very high. Under these conditions, the specific energy could be insufficient to produce a stable melt pool or to completely melt the incoming powder particles. As the deposition progresses, the temperature of the part gradually increases and the deposition is carried out on surfaces with a higher temperature compared to the initial temperature of the substrate. Therefore, the heat transfer becomes lower and the specific energy required to generate a stable deposition progressively decreases. In detail, the use of the laser power of $500\,\mathrm{W}$ provided less specific energy to the material and consequently the thermal energy was not enough to produce proper melt pool dimensions during the process. Hence, the values of the melt pool width or of the melt pool depth were not adequate for a good overlap between two consecutive tracks or between two consecutive layers. Figure 4b shows elongated lack-of-fusion pores in the bottom area, reflecting the deposition pattern and gradually fading along the growth direction. In Appendix A, specific cross-section views of this sample are reported.
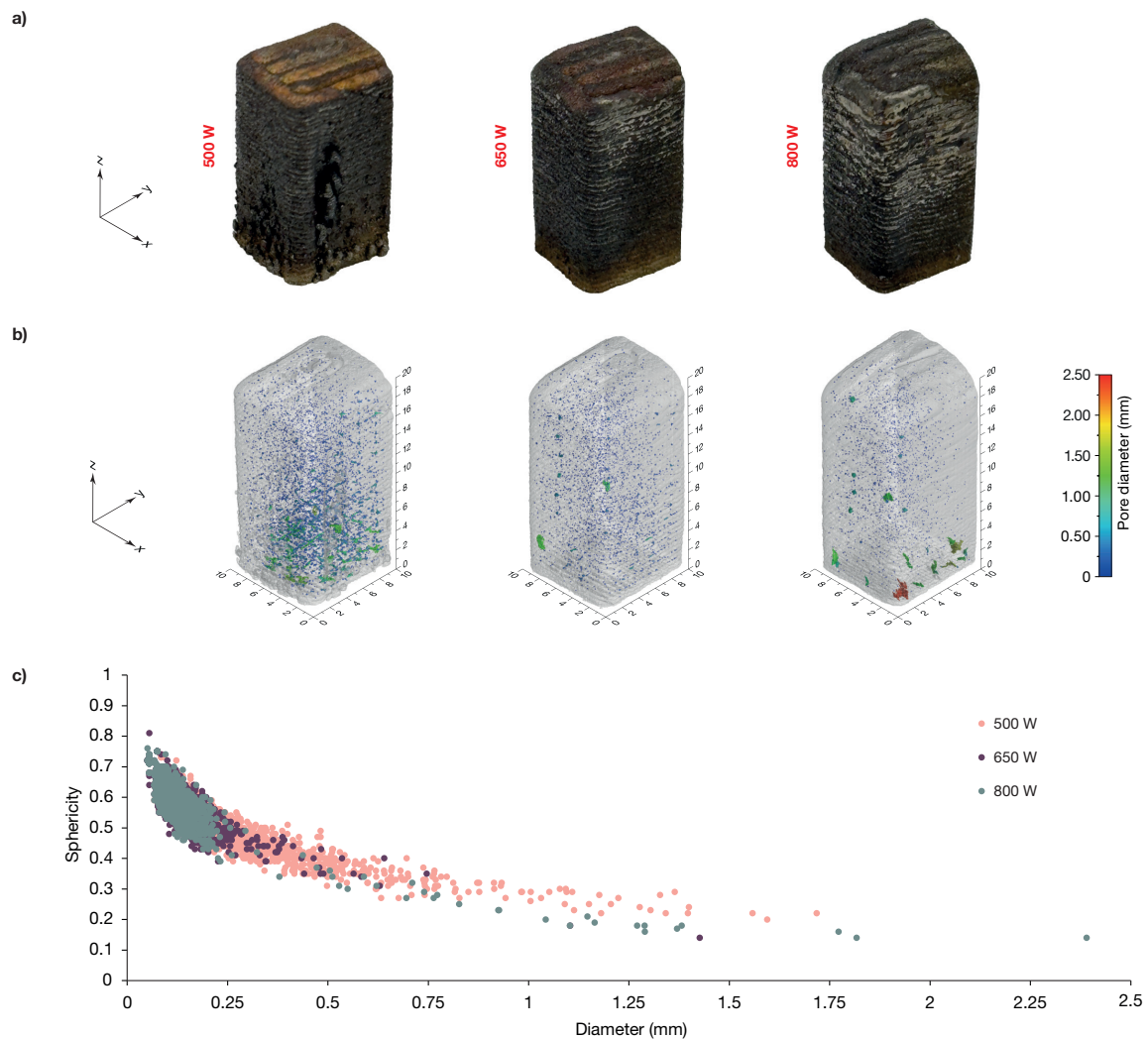
Figure 4. (a) Isometric view, (b) pore distribution, and (c) pore diameter vs sphericity of samples produced with different laser power values.

By increasing the laser power from 500 W to 650 W surface defects were minimized and internal porosity was dramatically reduced to 0.07 %. By analyzing the pores distribution, size and shape in Figure 4b and Figure 4c, the reduction of porosity value was attributed to a reduction of both gas-induced and lack-of-fusion pores.

By further increasing the laser power from 650 W to 800 W, the porosity level remained almost constant. However, when analyzing the pore characteristics in Figure 4b and Figure 4c, it was observed that the number of pores smaller than 0.3 mm decreased slightly while the number of pores with a size greater than 1 mm increased. These voids were mainly elongated along the building direction and located in the bottom area. They were thus attributed to the formation of hot cracks due to high stresses [38]. The formation of these cracks is in agreement with the findings of Huang et al. [39] and Lim et al. [40] which showed the tendency of the stainless steel to form cracks, especially in the edge of the sample and when high laser power values are used [40]. A more detailed representation of these defects is reported in Appendix A.

These results highlighted that, within the range of process parameters used in this work, a laser power of 650 W should be preferred, as a lower power level resulted in lack-of-fusion pores, while a higher laser power level resulted in the formation of hot cracks. This laser power value was thus selected for the next experiments.

3.1.2. Effect of Powder Mass Flow Rate

Figure 5a illustrates the second set of samples, produced with 650 W laser power, 850 mm/min travel speed and different values of powder mass flow rate. No visible defects, such as powder agglomerates, were present on the external surfaces of the samples. From the pore characteristics shown in Figure 5b and Figure 5c, it was observed that by increasing the powder mass flow rate from 4.5 g/min to 6.0 g/min, the porosity increased from 0.07 % to 0.10 % (Table 3). In all the samples both gas-induced pores, spherical and small, and lack-of-fusion pores, large and elongated, were detected. As a general consideration, it should be noted that by increasing the powder mass flow rate, the greater amount of powder delivered slightly reduces the useful power to melt the substrate, as more energy is absorbed, reflected and scattered by the incoming powder particles. Hence, for a constant value of specific energy, by increasing the powder mass flow rate a lower amount of thermal energy is available at the substrate.
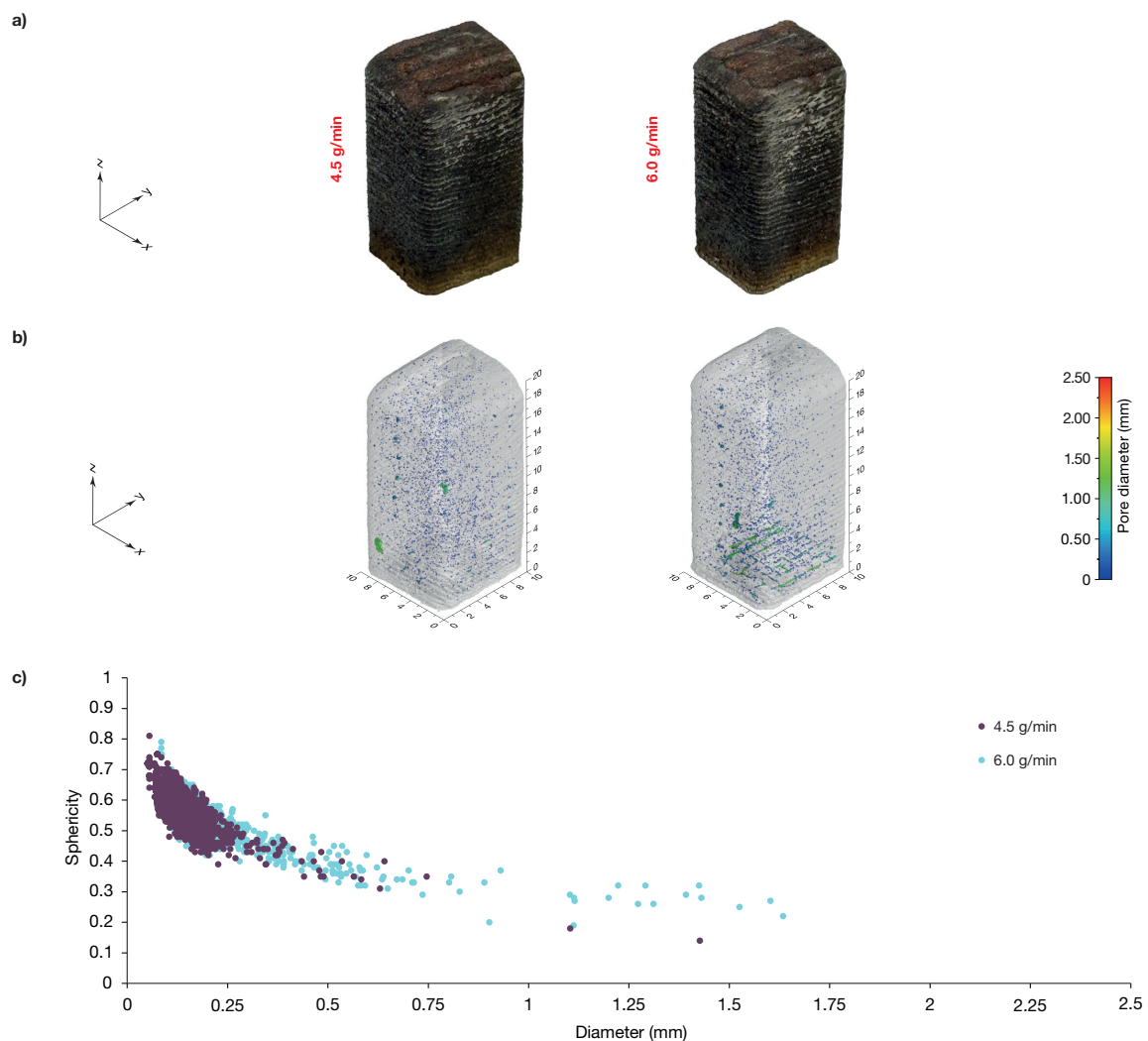

Figure 5. a) Isometric view, (b) pore distribution, and (c) pore diameter vs sphericity of samples produced with different powder mass flow rate values.

Gas-induced pores, which are intra-track porosities, were randomly distributed into the analyzed volume, and a slight reduction by increasing the powder mass flow rate was observed. The presence of gas-induced pores can be related to the Marangoni flows, which drive the gas pores towards the bottom of the melt pool preventing them from escaping [41]. The reduction of gas-induced pores moving from 4.5 g/min to 6.0 g/min, was related to a decrease in melt pool depth as the powder mass flow rate increased [42] according to Jeon et al. [43].

On the other hand, lack-of-fusion pores, which typically occur between two adjacent tracks, increased slightly and were concentrated in the first layers. This phenomenon can be attributed to the reduction in thermal energy available at the substrate as the powder mass flow rate is increased, coupled with the lower temperature in the initial layers, where steady-state conditions have not yet been reached and the temperature is lower. This has resulted in improper melt pool formation, with the fed material not having enough energy to be completely melted. Consequently lack-of-fusion pores developed and an increased number of pores was detected with a mean diameter bigger than 1 mm, as observed in Figure 5c.

Based on these results, it was possible to state that, within the range of process parameters used in this work, the use of the lower powder mass flow rate should be favored and for this reason, the value of 4.5 g/min was used in the subsequent analysis.

3.1.3. Effect of Travel Speed

Samples produced by setting $P = 650$ W, $Q_P = 4.5$ g/min and by varying the travel speed are shown in Figure 6a. No visible defects were observed on the external surfaces. The spatial distribution of porosity inside samples is illustrated in Figure 6b. In general, the porosity level was not influenced by the travel speed value and remained almost constant with an average value of 0.07 %. Specifically, both gas-induced pores and lack-of-fusion pores appeared to be insensitive to travel speed values. In fact, aFigure 6c shows that the distribution of pores sphericity over their diameter was almost the same for all the samples.

Based on the obtained results, it was possible to observe that, within the range of process parameters analyzed in this work, the value of travel speed did not modify the porosity of the samples and consequently, the porosity cannot be used as a discriminator parameter for the selection of travel speed value.

However, it should be noted that process parameters, and hence also the value of travel speed, significantly influence the mechanical properties and the tolerances of the produced part [5,8,29]. For instance, in previous work, the authors showed that a lower travel speed value led to a lower value of residual stress [44], and Zhang et al. [45] observed that a lower value of travel speed corresponds to lower mechanical characteristics in terms of yield strength and elongation.
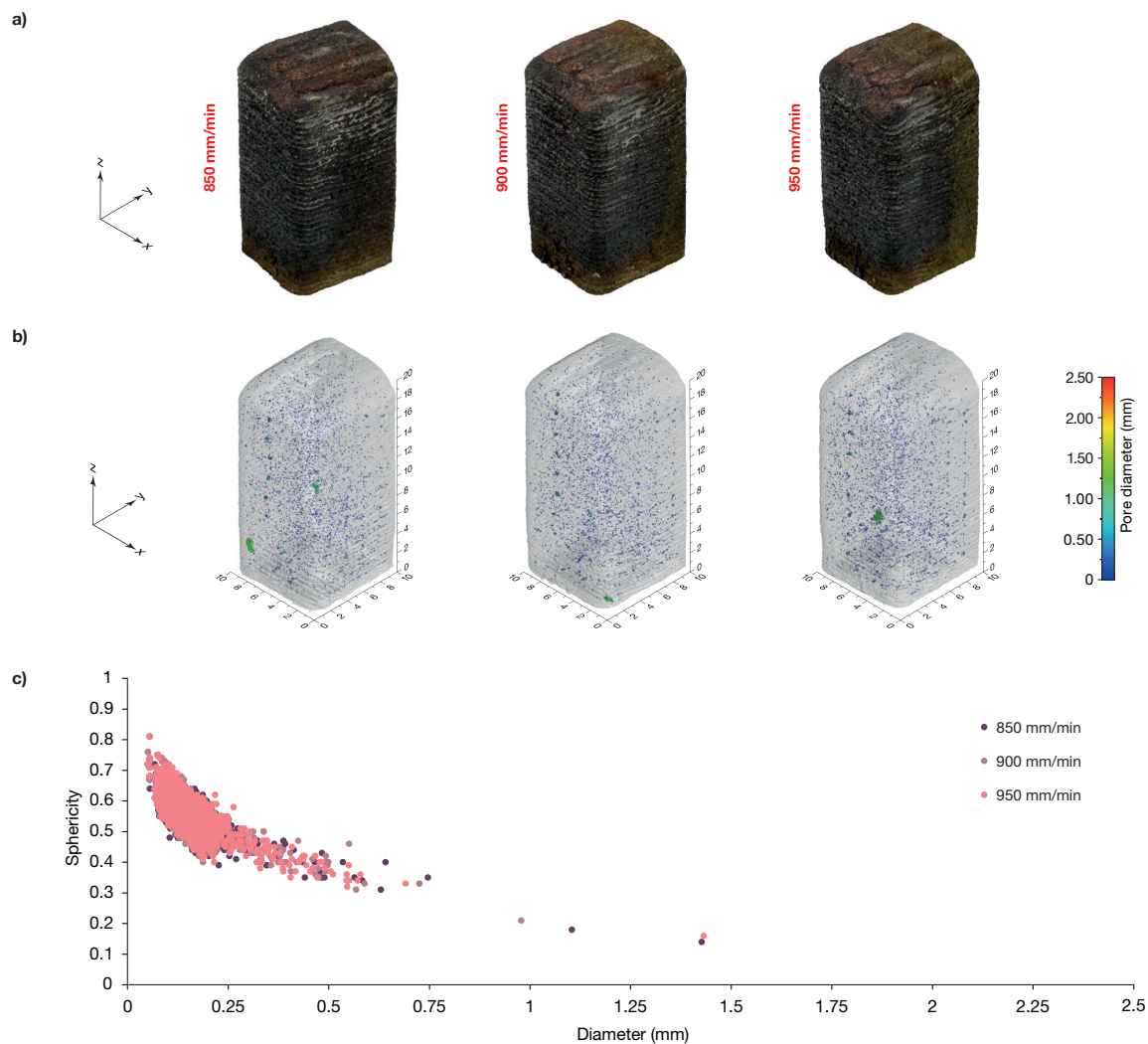
Figure 6. (a) Isometric view, (b) pore distribution and (c) pore diameter vs sphericity of samples produced with different travel speed values.

3.2. Temperature Distribution

In the following paragraphs, the results obtained from the numerical simulation are presented and correlated to the experimental results. The simulations were carried out using an HP Z4 G8 workstation equipped with two Intel® Xeon® Gold 5222 processors at 3.8 GHz and 256 GB of RAM memory using four CPUs. The duration of the simulations was dependent on the process parameters used, with a maximum of 72 h.

Since from the experiments it was observed that the laser power was the most relevant parameter on porosities, the results of the thermal numerical simulation are presented for the conditions of Set 1. Figure 7 shows the temperature distribution in the cross-sections of the samples of Set 1 when the track is advancing in the middle of the 15th layer, at a height of 7.5 mm. From the temperature maps, it is possible to observe that the laser power value significantly influences the temperature distribution into the deposited material, with the peak temperature increasing by 13 % when the laser power rises from 500 W to 650 W. In addition, a larger affected area is evidenced by the isothermal curve at 673 K (used as reference since carbide precipitation does not occur at lower temperatures). This isothermal curve was represented by the white dotted line in Figure 7. By further increasing the laser power to 800 W, the effect is intensified and is increasingly pronounced in depth mainly due to conductive heat transfer. Temperatures in the substrate are in general lower due to the thermal inertia and convective

phenomena on top and bottom surfaces, evidencing a significant thermal rise on the bottom surface when the laser power reaches 800 W.
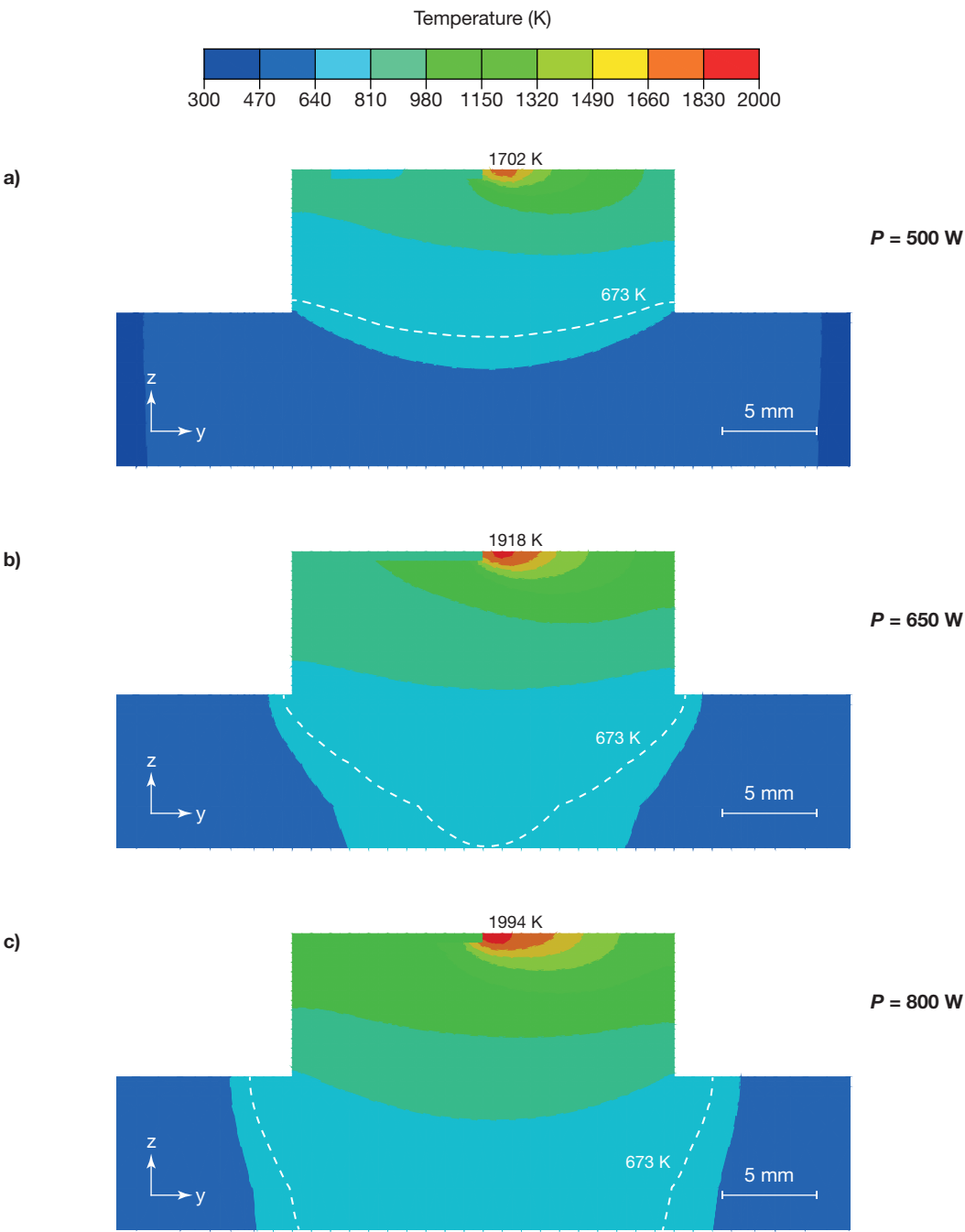

Figure 7. Temperature distribution obtained from numerical FE model when the track is advancing in the middle of the 15th layer, in samples produced with different laser power: (a) 500 W, (b) 650 W and (c) 800 W.

3.2.1. Correlation between Temperature and Lack-of-Fusion Porosity

The temperature of the node at the center of the interface surface between the deposit and the substrate (node N in the Figure 8b) was extracted from the FE thermal simulation output as a function of time. This temperature history was then correlated to the presence of porosities, especially lack-of-fusion, as detected by computed tomography in the samples of Set 1. From Figure 8a it is possible to observe that in each sample of Set 1 three different volumes can be identified. The lowermost volume is characterized by a greater concentration of pores and elongated defects. This volume will hereafter be referred to as the lack-of-fusion pores volume. The porosity and defects decreased progressively in the *Transition volume*, which involved approximately four to six layers. This was followed by an almost uniform porosity, which was mainly comprised of gas-induced pores. This volume is identified as the *low porosity volume*. Looking at the sample produced with a laser power of 500 W, that is the most porous sample, it is possible to restrict the *Lack-of-fusion pore volume* to the first 10 layers corresponding to a height of approximately 5 mm. Above 9 mm of height, that is from the 18ᵗʰ layer, the *transition volume* is exceeded.
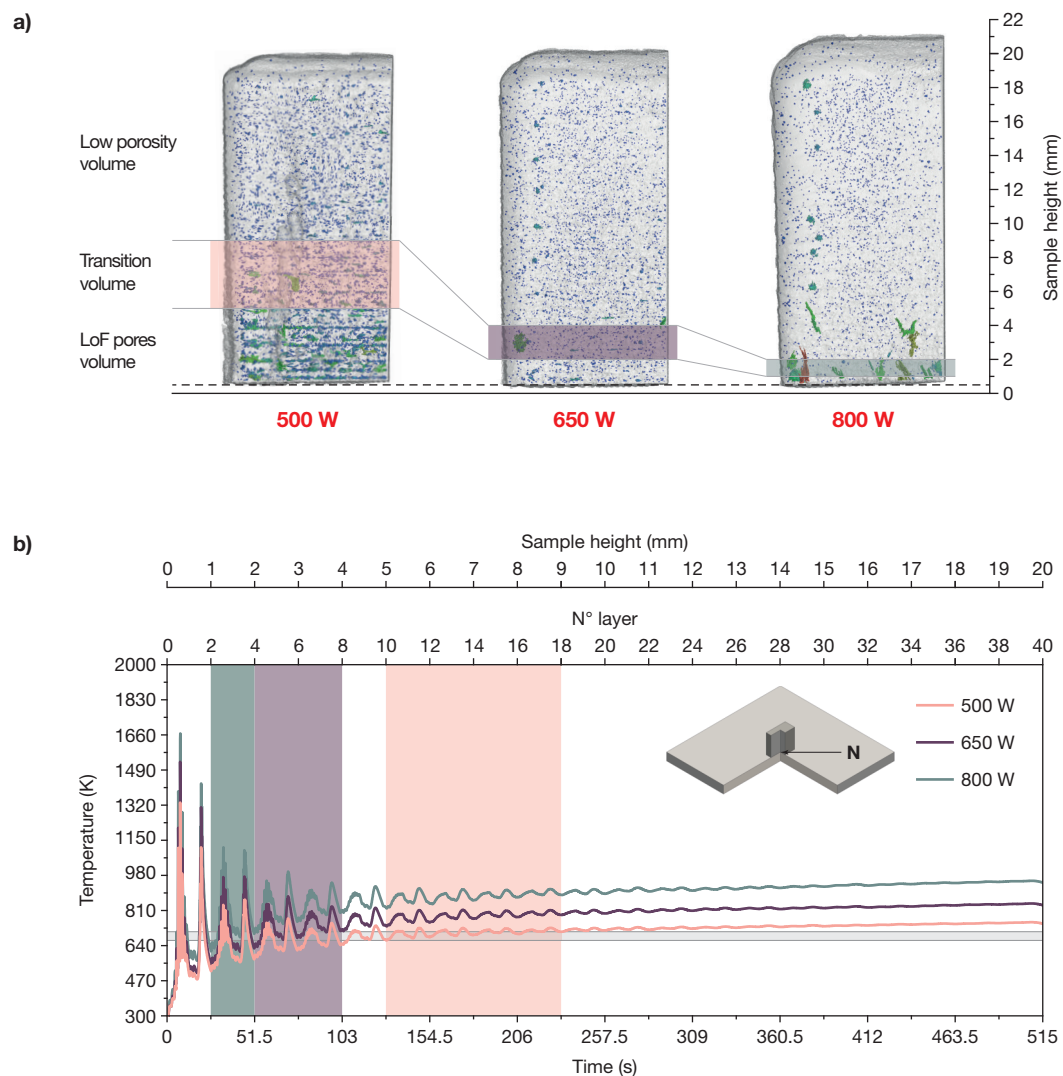

Figure 8. (a) Side view of the CT analysis results and (b) temperature distribution extracted from FE numerical model in the samples of Set 1. The pink, purple and dark green boxes indicate the transition volume in the sample produced at 500 W, 650 W, and 800 W respectively. The gray box define the temperature interval in the transition volumes.

By comparing these observations with the temperature history extracted on node N of the sample, it is possible to infer a correlation. In detail, in the first 10 layers the temperature at the end of each thermal cycle (that is when all the tracks of a single layer are deposited) is progressively rising towards a steady state condition, that is almost reached at the 18th layer. In the transition layers (11th to 18th layers), the thermal cycles are clearly visible. However, the temperature rise after each thermal cycle is significantly reduced in comparison to the previous layers. The temperatures reached after the deposition of the 10th and 18th layers, 665 K and 707 K, respectively, were extracted as the temperatures that define the transition zone. Subsequently, for the other two samples produced at higher laser power, the layers at which the same limit temperatures are reached at the end of a thermal cycle were identified and then analyzed in the computed tomography results. This was done to verify whether the transient volume was effectively evidenced in the intermediate layers.

Considering the sample produced at 650 W of laser power, the analysis suggested a transition volume between the 4th and 8th layers. This indication is verified by the experimental evidence, with lack-of-fusion pores present below this volume and absent above. Two large porosities were detected in the transition volume and were attributed to inter-track porosities between the contour and the core deposition tracks. Agreement between the temperature history and experimental results was found also in the sample produced at 800 W of laser power, with the transition zone located from the 2nd and the 4th layers. However, the detected defects, aligned along the building direction, were recognized as cracks rather than lack-of-fusion pores.

The comparison conducted between the results of the numerical simulation, which identified the volume where lack-of-fusion pores/defects were likely to be present, and the experimental results from the CT analysis, allows for some conclusions to be drawn. The findings demonstrated that the numerical model was capable of predicting the presence of lack-of-fusion pores or defects along the building direction, with an average error of approximately 0.5 mm (1 layer).

4. Conclusions

In this work, the effect on porosity of the main process parameters of the DED-LB/Powder process, namely laser power, powder mass flow rate and travel speed, was investigated. Results showed that all the samples were characterized by a porosity level lower than 0.26 % and that this value was mainly influenced by laser power. In addition, two main pore types were identified which are the gas-induced pores, uniformly distributed in the volume, and the lack-of-fusion pores, which were mainly located in the bottom part of the samples. Then, a transient macro-scale numerical model was developed with the purpose of analyzing the thermal history. The main results can be summarized as follows:

- The laser power had the higher influence on porosity. Increasing laser power has a beneficial effect in reducing porosity. However, excessive laser power could lead to the formation of cracks at the interface with the substrate;
- The powder mass flow rate influenced both gas-induced pores and lack-of-fusion pores. In detail, the increase of powder mass flow rate led to a reduction of gas-induced pores and this was related to the reduction of melt pool depth. On the other hand, the lack-of-fusion pores increased due to the melt pool width reduction;
- The travel speed had no significant influence on the porosity level with deviations in line with the process variability;
- A correlation was found between the thermal history and the presence and position of lack-of-fusion pores. This suggests that the numerical model can be a useful tool to predict the presence of such porosity.

Abbreviations

The following abbreviations are used in this manuscript:

AM	Additive Manufacturing
DED	Directed Energy Deposition
PBF	Powder Bed Fusion
DED-LB/Powder	Powder Laser Beam Directed Energy Deposition
CT	Computed Tomography
FE	Finite Element

Appendix A. Detailed Cross-Section Views for Porosity Analysis

Figure A1 shows different cross-section views of the sample produced with a laser power of 500 W, a travel speed of 650 mm/min, and a powder mass flow rate of 4.5 g/min. Figure A1a and Figure A1b show the cross-section perpendicular to the y-axis (Cross-section Σ) and the cross-section perpendicular to x-axis (Cross-section Ψ), respectively. From these sections, it was possible to verify that the lack-of-fusion pores were aligned with the deposition path.

Figure A2 shows some relevant cross-section views obtained in the sample produced with a laser power of 800 W, a travel speed of 650 mm/min and a powder mass flow rate of 4.5 g/min. In fact, the analysis reported in paragraph 3.1.1, revealed that some cracks developed in the bottom zone of this sample. Consequently, a further characterization of the defects was developed, in order to understand the significance of these cracks.

From Figure A2a and Figure A2b, which represent two perpendicular cross-sections along the building direction of the sample, it was possible to observe that the cracks were elongated along the building direction and they developed starting from the W-EDM cutting plane.

In Figure A1c two cross-sections perpendicular to the building direction are represented. In the lowermost section (Cross-section Ω_2), located at a height of about 1.2 mm, the large amount of lack-of-fusion pores is clearly visible. In the cross-section Ω_1, obtained at a distance of 4.6 mm, the lack-of-fusion pores are significantly reduced. In addition, these sections highlight the irregularities on the lateral surface caused by the low specific energy.

Figure A2c shows cross-section views perpendicular to the building direction obtained at two different heights of the sample. The cross-section Ω_2 obtained at a distance of about 1.3 mm from the building platform, revealed that these cracks were present on almost all the surface, however as discussed in paragraph 3.1.1 they were more pronounced on the external areas of the sample. On the other hand, the cross-section Ω_1, obtained at a distance of 3.8 mm, was free of defects.
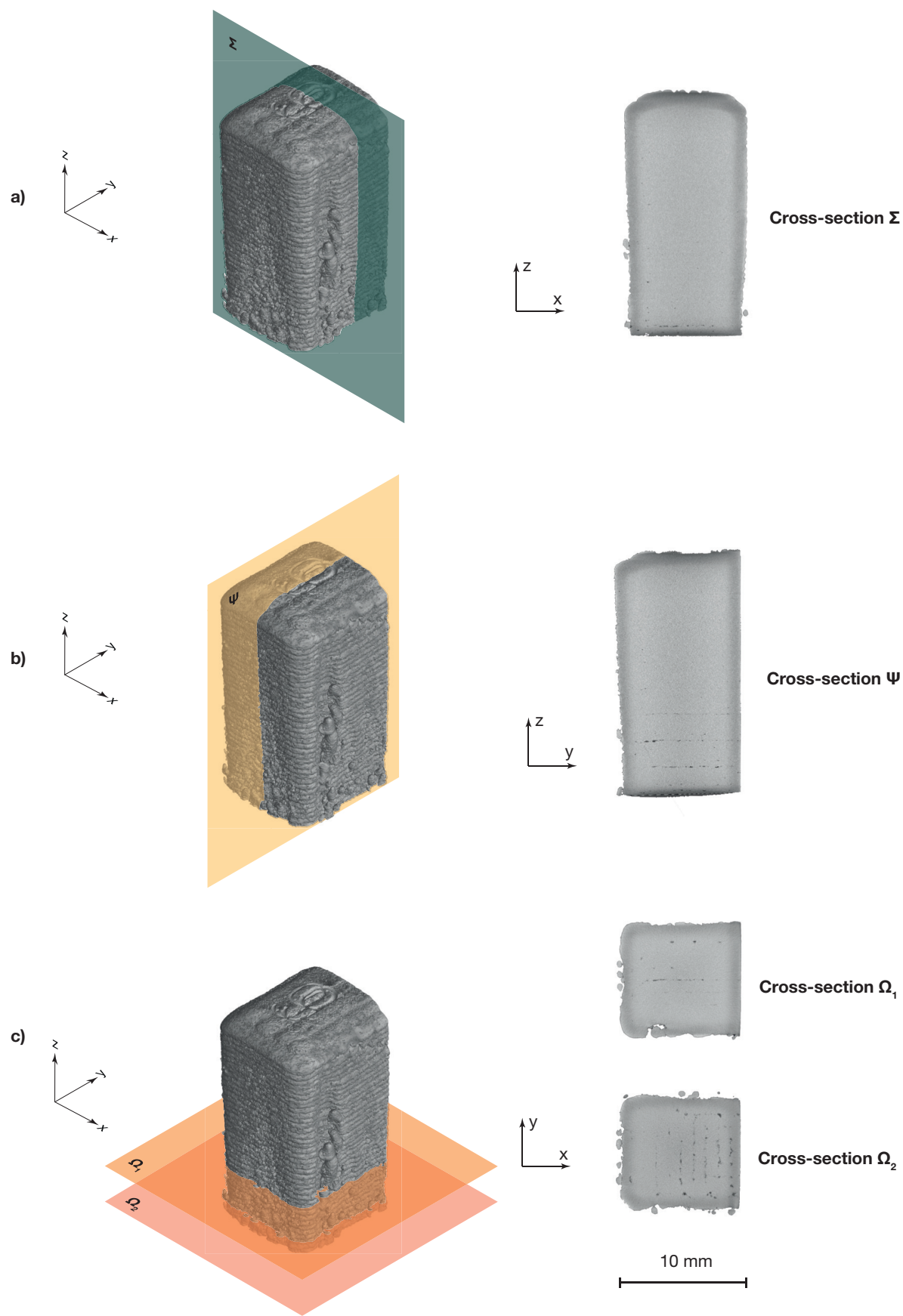
Figure A1. Cross-section views in the sample produced with a laser power of 500 W, a travel speed of 850 mm/min and a powder mass flow rate of 4.5 g/min.
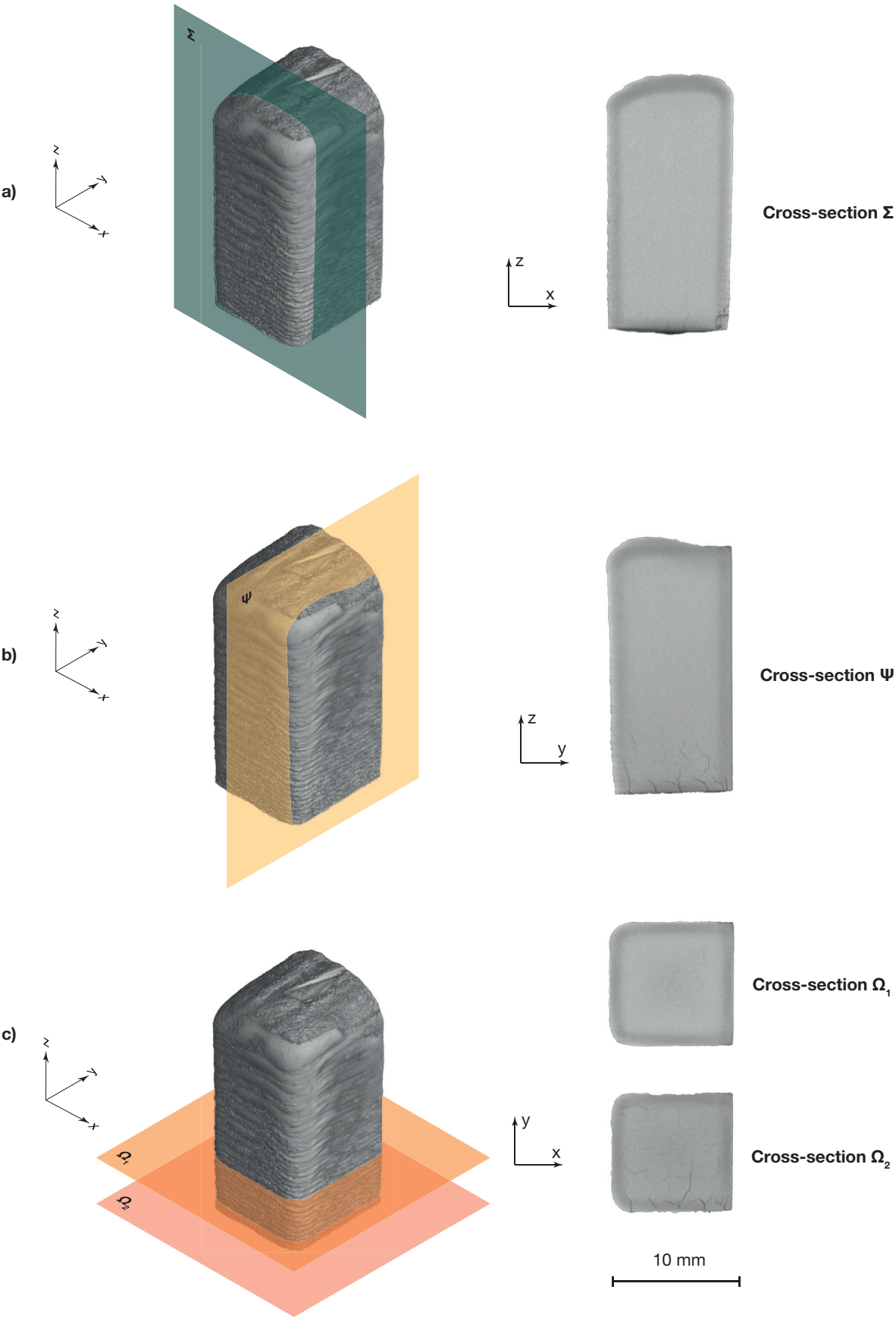
Figure A2. Cross-section views in the sample produced with a laser power of 800 W, a travel speed of 850 mm/min and a powder mass flow rate of 4.5 g/min.

References

1. Praveena, B.; Lokesh, N.; Buradi, A.; Santhosh, N.; Praveena, B.L.; Vignesh, R. A comprehensive review of emerging additive manufacturing (3D printing technology): Methods, materials, applications, challenges, trends and future potential. *Materials Today: Proceedings* **2022**, *52*, 1309–1313. doi:10.1016/j.matpr.2021.11.059.

2. Bandyopadhyay, A.; Traxel, K.D.; Lang, M.; Juhasz, M.; Eliaz, N.; Bose, S. Alloy design via additive manufacturing: Advantages, challenges, applications and perspectives. *Materials Today* **2022**, *52*, 207–224. doi:10.1016/j.mattod.2021.11.026.

3. Ampower GmbH & Co. KG. Metal Additive Manufacturing Report. AMPOWER Report 2020, 2020. Available online: http://www.additive-manufacturing-report.com (accessed on 27-01-2021).

4. Ahn, D.G. Directed Energy Deposition (DED) Process: State of the Art. *International Journal of Precision Engineering and Manufacturing - Green Technology* **2021**, *8*, 703–742. doi:10.1007/s40684-020-00302-7.

5. Izadi, M.; Farzaneh, A.; Mohammed, M.; Gibson, I.; Rolfe, B. A review of laser engineered net shaping (LENS) build and process parameters of metallic parts. *Rapid Prototyping Journal* **2020**, *26*, 1059–1078. doi:10.1108/Rpj-04-2018-0088.

6. ASTM International, West Conshohocken, PA. *Standard Guide for Directed Energy Deposition of Metals*, 2016. Available online: https://www.astm.org/f3187-16.html (accessed on 25-04-2024).

7. Piscopo, G.; Iuliano, L. Current research and industrial application of laser powder directed energy deposition. *International Journal of Advanced Manufacturing Technology* **2022**, *119*, 6893–6917. doi:10.1007/s00170-021-08596-w.

8. Piscopo, G.; Atzeni, E.; Saboori, A.; Salmi, A. An Overview of the Process Mechanisms in the Laser Powder Directed Energy Deposition. *Applied Sciences (Switzerland)* **2023**, *13*. doi:10.3390/app13010117.

9. Sohn, H.; Liu, P.; Yoon, H.; Yi, K.; Yang, L.; Kim, S. Real-time porosity reduction during metal directed energy deposition using a pulse laser. *Journal of Materials Science & Technology* **2022**, *116*, 214–223. doi:10.1016/j.jmst.2021.12.013.

10. Al-Maharma, A.Y.; Patil, S.P.; Markert, B. Effects of porosity on the mechanical properties of additively manufactured components: a critical review. *Materials Research Express* **2020**, *7*. doi:10.1088/2053-1591/abcc5d.

11. Tan, Z.E.; Pang, J.H.L.; Kaminski, J.; Pepin, H. Characterisation of porosity, density, and microstructure of directed energy deposited stainless steel AISI 316L. *Additive Manufacturing* **2019**, *25*, 286–296. doi:10.1016/j.addma.2018.11.014.

12. Svetlizky, D.; Das, M.; Zheng, B.; Vyatskikh, A.L.; Bose, S.; Bandyopadhyay, A.; Schoenung, J.M.; Lavernia, E.J.; Eliaz, N. Directed energy deposition (DED) additive manufacturing: Physical characteristics, defects, challenges and applications. *Materials Today* **2021**, *49*, 271–295. doi:10.1016/j.mattod.2021.03.020.

13. DebRoy, T.; Wei, H.L.; Zuback, J.S.; Mukherjee, T.; Elmer, J.W.; Milewski, J.O.; Beese, A.M.; Wilson-Heid, A.; De, A.; Zhang, W. Additive manufacturing of metallic components – Process, structure and properties. *Progress in Materials Science* **2018**, *92*, 112–224. doi:10.1016/j.pmatsci.2017.10.001.

14. Chen, L.; Yao, X.; Tan, C.; He, W.; Su, J.; Weng, F.; Chew, Y.; Ng, N.P.H.; Moon, S.K. In-situ crack and keyhole pore detection in laser directed energy deposition through acoustic signal and deep learning. *Additive Manufacturing* **2023**, *69*. doi:10.1016/j.addma.2023.103547.

15. Wolff, S.J.; Wang, H.; Gould, B.; Parab, N.; Wu, Z.; Zhao, C.; Greco, A.; Sun, T. In situ X-ray imaging of pore formation mechanisms and dynamics in laser powder-blown directed energy deposition additive manufacturing. *International Journal of Machine Tools and Manufacture* **2021**, *166*. doi:10.1016/j.ijmachtools.2021.103743.

16. Svetlizky, D.; Zheng, B.; Buta, T.; Zhou, Y.; Golan, O.; Breiman, U.; Haj-Ali, R.; Schoenung, J.M.; Lavernia, E.J.; Eliaz, N. Directed energy deposition of Al 5xxx alloy using Laser Engineered Net Shaping (LENS®). *Materials & Design* **2020**, *192*. doi:10.1016/j.matdes.2020.108763.

17. Dass, A.; Moridi, A. State of the Art in Directed Energy Deposition: From Additive Manufacturing to Materials Design. *Coatings* **2019**, *9*. doi:10.3390/coatings9070418.

18. Susan, D.F.; Puskar, J.D.; Brooks, J.A.; Robino, C.V. Quantitative characterization of porosity in stainless steel LENS powders and deposits. *Materials Characterization* **2006**, *57*, 36–43. doi:10.1016/j.matchar.2005.12.005.

19. Ahsan, M.N.; Bradley, R.; Pinkerton, A.J. Microcomputed tomography analysis of intralayer porosity generation in laser direct metal deposition and its causes. *Journal of Laser Applications* **2011**, *23*. doi:10.2351/1.3582311.

20. Rahman Rashid, R.A.; Abaspour, S.; Palanisamy, S.; Matthews, N.; Dargusch, M.S. Metallurgical and geometrical characterisation of the 316L stainless steel clad deposited on a mild steel substrate. *Surface and Coatings Technology* **2017**, *327*, 174–184. doi:10.1016/j.surfcoat.2017.08.013.

21. Zheng, B.; Haley, J.C.; Yang, N.; Yee, J.; Terrassa, K.W.; Zhou, Y.; Lavernia, E.J.; Schoenung, J.M. On the evolution of microstructure and defect control in 316L SS components fabricated via directed energy deposition. *Materials Science and Engineering: A* **2019**, *764*, 138243. doi:10.1016/j.msea.2019.138243.

22. Mahamood, R.M.; Akinlabi, E.T., Modelling of Process Parameters Influence on Degree of Porosity in Laser Metal Deposition Process. In *Transactions on Engineering Technologies*; Springer Netherlands, 2015; book section Chapter 3, pp. 31–42. doi:10.1007/978-94-017-9588-3_3.

23. Amar, E.; Popov, V.; Sharma, V.M.; Andreev Batat, S.; Halperin, D.; Eliaz, N. Response Surface Methodology (RSM) Approach for Optimizing the Processing Parameters of 316L SS in Directed Energy Deposition. *Materials* **2023**, *16*. doi:10.3390/ma16237253.

24. Majumdar, J.D.; Pinkerton, A.; Liu, Z.; Manna, I.; Li, L. Microstructure characterisation and process optimization of laser assisted rapid fabrication of 316L stainless steel. *Applied Surface Science* **2005**, *247*, 320–327. doi:10.1016/j.apsusc.2005.01.039.

25. Lin, P.Y.; Shen, F.C.; Wu, K.T.; Hwang, S.J.; Lee, H.H. Process optimization for directed energy deposition of SS316L components. *The International Journal of Advanced Manufacturing Technology* **2020**, *111*, 1387–1400. doi:10.1007/s00170-020-06113-z.

26. Kartikeya Sarma, I.; Srinivas, V.; Kanmani Subbu, S. Effect of process parameters on micro hardness, bulk hardness and porosity of LENSTM deposited SS 316L alloy. *Materials Today: Proceedings* **2021**, *46*, 2616–2624. doi:10.1016/j.matpr.2021.02.268.

27. Savitha, U.; Reddy, G.J.; Venkataramana, A.; Gokhale, A.A.; Sundararaman, M. Effect of Process Parameters on Solidification Structure and Properties of Laser Deposited SS316 Alloy. *Transactions of the Indian Institute of Metals* **2015**, *68*, 1017–1022. doi:10.1007/s12666-015-0638-1.

28. Thompson, S.M.; Bian, L.; Shamsaei, N.; Yadollahi, A. An overview of Direct Laser Deposition for additive manufacturing; Part I: Transport phenomena, modeling and diagnostics. *Additive Manufacturing* **2015**, *8*, 36–62. doi:10.1016/j.addma.2015.07.001.

29. Gibson, I.; Rosen, D.; Stucker, B. *Directed Energy Deposition Processes*, 2nd ed.; Springer: New York, 2015; book section Chapter 10, pp. 245–268. doi:10.1007/978-1-4939-2113-3_10.

30. Piscopo, G.; Atzeni, E.; Salmi, A.; Iuliano, L.; Gatto, A.; Marchiandi, G.; Balestrucci, A. Mesoscale modelling of laser powder-based directed energy deposition process. 2020, Vol. 88, pp. 393–398. doi:10.1016/j.procir.2020.05.068.

31. Guan, X.; Zhao, Y.F. Modeling of the laser powder–based directed energy deposition process for additive manufacturing: a review. *The International Journal of Advanced Manufacturing Technology* **2020**, *107*, 1959–1982. doi:10.1007/s00170-020-05027-0.

32. Vincic, J. Laser Directed Energy Deposition for Processing and Repairing Steels. PhD thesis, Politecnico di Torino, 2024.

33. Piscopo, G.; Salmi, A.; Atzeni, E. Investigation of dimensional and geometrical tolerances of laser powder directed energy deposition process. *Precision Engineering* **2024**, *85*, 217–225. doi:10.1016/j.precisioneng.2023.10.006.

34. Piscopo, G.; Atzeni, E.; Salmi, A. A Hybrid Modeling of the Physics-Driven Evolution of Material Addition and Track Generation in Laser Powder Directed Energy Deposition. *Materials* **2019**, *12*. doi:10.3390/ma12172819.

35. Unocic, R.R.; DuPont, J.N. Process efficiency measurements in the laser engineered net shaping process. *Metallurgical and Materials Transactions B* **2004**, *35*, 143–152. doi:10.1007/s11663-004-0104-7.

36. Gouge, M.F.; Heigel, J.C.; Michaleris, P.; Palmer, T.A. Modeling forced convection in the thermal simulation of laser cladding processes. *The International Journal of Advanced Manufacturing Technology* **2015**, *79*, 307–320. doi:10.1007/s00170-015-6831-x.

37. Yadav, S.; Paul, C.; Jinoop, A.; Rai, A.; Bindra, K. Laser Directed Energy Deposition based Additive Manufacturing of Copper: Process Development and Material Characterizations. *Journal of Manufacturing Processes* **2020**, *58*, 984–997. doi:10.1016/j.jmapro.2020.09.008.

38. Zhang, W.; Xu, C.; Li, C.; Wu, S. Advances in Ultrasonic-Assisted Directed Energy Deposition (DED) for Metal Additive Manufacturing. *Crystals* **2024**, *14*. doi:10.3390/cryst14020114.

39. Huang, G.; Wei, K.; Deng, J.; Liu, M.; Zeng, X. High-power laser powder bed fusion of 316L stainless steel: Defects, microstructure, and mechanical properties. *Journal of Manufacturing Processes* **2022**, *83*, 235–245. doi:10.1016/j.jmapro.2022.08.066.

40. Lim, S.H.; Ryou, K.; Jang, K.; Choi, W.S.; Lee, H.M.; Choi, P.P. Hot cracking behavior of additively manufactured D2 steel. *Materials Characterization* **2021**, *178*. doi:10.1016/j.matchar.2021.111217.

41. Bennett, J.; Webster, S.; Byers, J.; Johnson, O.; Wolff, S.; Ehmann, K.; Cao, J. Powder-borne porosity in directed energy deposition. *Journal of Manufacturing Processes* **2022**, *80*, 69–74. doi:10.1016/j.jmapro.2022.04.036.

42. Biyikli, M.; Karagoz, T.; Calli, M.; Muslim, T.; Ozalp, A.A.; Bayram, A. Single Track Geometry Prediction of Laser Metal Deposited 316L-Si Via Multi-Physics Modelling and Regression Analysis with Experimental Validation. *Metals and Materials International* **2022**, *29*, 807–820. doi:10.1007/s12540-022-01243-3.

43. Jeon, I.; Liu, P.; Sohn, H. Real-time melt pool depth estimation and control during metal-directed energy deposition for porosity reduction. *The International Journal of Advanced Manufacturing Technology*. doi:10.1007/s00170-023-11689-3.

44. Piscopo, G.; Salmi, A.; Atzeni, E. Influence of High-Productivity Process Parameters on the Surface Quality and Residual Stress State of AISI 316L Components Produced by Directed Energy Deposition. *Journal of Materials Engineering and Performance* **2021**, *30*, 6691–6702. doi:10.1007/s11665-021-05954-3.

45. Zhang, K.; Wang, S.; Liu, W.; Shang, X. Characterization of stainless steel parts by Laser Metal Deposition Shaping. *Materials & Design* **2014**, *55*, 104–119. doi:10.1016/j.matdes.2013.09.006.